Available online at www.sciencedirect.com

SciVerse ScienceDirect

Acta Materialia 60 (2012) 3643–3654

Acta MATERIALIA

www.elsevier.com/locate/actamat

Effect of Er additions on ambient and high-temperature strength of precipitation-strengthened Al–Zr–Sc–Si alloys

Christopher Booth-Morrison [a], David N. Seidman [a,b], David C. Dunand [a,*]

[a] Department of Materials Science and Engineering, Northwestern University, Evanston, IL 60208-3108, USA
[b] Northwestern University Center for Atom-Probe Tomography (NUCAPT), Evanston, IL 60208-3108, USA

Received 25 July 2011; received in revised form 14 February 2012; accepted 16 February 2012
Available online 7 April 2012

Abstract

The effect of substituting 0.01 at.% Er for Sc in an Al–0.06Zr–0.06Sc–0.04Si (at.%) alloy subjected to a two-stage aging treatment (4 h/300 °C and 8 h/425 °C) is assessed to determine the viability of dilute Al–Si–Zr–Sc–Er alloys for creep applications. Upon aging, coherent, 2–3 nm radius, $L1_2$-ordered, trialuminide precipitates are created, consisting of an Er- and Sc-enriched core and a Zr-enriched shell; Si partitions to the precipitates without preference for the core or the shell. The Er substitution significantly improves the resistance of the alloy to dislocation creep at 400 °C, increasing the threshold stress from 7 to 10 MPa. Upon further aging under an applied stress for 1045 h at 400 °C, the precipitates grow modestly to a radius of 5–10 nm, and the threshold stress increases further to 14 MPa. These chemical and size effects on the threshold stress are in qualitative agreement with the predictions of a recent model, which considers the attractive interaction force between mismatching, coherent precipitates and dislocations that climb over them. Micron-size, intra- and intergranular, blocky Al_3Er precipitates are also present, indicating that the solid solubility of Er in Al is exceeded, leading to a finer-grained microstructure, which results in diffusional creep at low stresses.

Keywords: Aluminum alloys; Precipitation; Scandium; Zirconium; Erbium

1. Introduction

Dilute Al–Zr–Sc–Er alloys have recently been demonstrated to offer an attractive combination of high-temperature creep resistance, coarsening resistance and affordability, the latter because they are castable and heat-treatable [1]. These alloys are excellent candidates to replace much heavier (but less costly) iron-based alloys and heavier (and much costlier) titanium alloys for automotive and aerospace parts exposed to intermediate temperatures (250–400 °C) and low stresses (<20 MPa). With appropriate aging treatments, Al–Zr–Sc–Er alloys form coherent, spheroidal, $L1_2$-ordered precipitates that remain coarsening resistant for >64 days at 400 °C, owing to a structure consisting of an Er-enriched core surrounded by a Sc-enriched inner shell and a Zr-enriched outer shell [1]. This core/double-shell structure is formed as solute elements precipitate sequentially, according to their intrinsic diffusivities D in the aluminum matrix, where $D_{Er} > D_{Sc} > D_{Zr}$. In the absence of Er, dilute Al–Sc–Zr alloys form coarsening-resistant $L1_2$-ordered precipitates, which consist of a Sc-enriched core surrounded by a Zr-enriched shell [1–15]. The substitution of some of the Sc with the much lower-cost Er has proved effective in improving the creep resistance of Al–Sc alloys at 300 °C, while maintaining their coarsening resistance [16–18]. Erbium is the least expensive of the heavy rare-earth elements (RE) that form $L1_2$ precipitates in aluminum [19], and Al_3Er ($L1_2$) has the largest lattice parameter misfit with Al ($\delta = +4.08\%$ at room temperature) [20], thereby improving creep resistance by enhancing elastic interactions with dislocations [17,21,22].

It was shown previously that an alloy composition of Al–0.06Zr–0.04Sc–0.02Er (at.%) provides a desirable combination of strength, coarsening resistance and affordability [1].

* Corresponding author.
E-mail address: dunand@northwestern.edu (D.C. Dunand).

1359-6454/$36.00 © 2012 Acta Materialia Inc. Published by Elsevier Ltd. All rights reserved.
doi:10.1016/j.actamat.2012.02.030

The Al–Zr–Sc–Er alloys in this previous study were, however, found to have intragranular Al_3Zr flakes retained from the melt as a result of incomplete dissolution of the Al–Zr master alloy, and intergranular Al_3Er ($L1_2$) precipitates formed during solidification and/or homogenization, because the limited matrix solubility of Er was exceeded [1]. These particles lowered the effective solute concentration of the alloys, reducing the precipitate volume fraction, and limiting alloy strength. These issues are addressed here by induction-melting of the alloys to ensure complete dissolution of Al_3Zr present in the master alloy, and by employing a lower Er concentration of 0.01 at.% to compare with the base Al–0.06Zr–0.06Sc–0.04Si alloy. Silicon was added intentionally to accelerate the precipitation kinetics of Sc, so that peak strength from Al_3Sc ($L1_2$) precipitates at 300 °C could be achieved after only 4 h [23]. A two-stage aging treatment of 24 h at 300 °C, followed by 8 h at 400 °C, was previously shown to provide peak strength in Al–0.06Zr–0.06Sc and Al–0.06Zr–0.04Sc–0.02Er (at.%), where Si was not controlled, but present naturally at <0.005 at.% [1].

The focus here is on the mechanical properties of Al–0.06Zr–0.06Sc–0.04Si and Al–0.06Zr–(0.05Sc–0.01Er)–0.04Si (at.%). at ambient and elevated temperature to determine the viability of these modified compositions (additional Si and reduced Er compared with Al–0.06Zr–0.04Sc–0.02Er (at.%) [1]) in high-temperature, low-stress, applications. The effect of substituting 0.01 at.% Er for Sc on the microstructure, precipitate nanostructure and creep resistance of the alloys following aging to peak ambient temperature strength is studied by scanning electron microscopy (SEM), atom-probe tomography (APT), microhardness and creep testing.

2. Experimental procedures

2.1. Alloy compositions and processing

Alloys with nominal compositions of Al–0.06Zr–0.06Sc–0.04Si and Al–0.06Zr–(0.05Sc–0.01Er)–0.04Si (at.%) (Al–0.2Zr–0.1 Sc–0.04Si and Al–0.2Zr–(0.08Sc–0.06Er)–0.04Si wt.%) were inductively melted to a temperature of 900 °C from 99.99 at.% pure Al, 99.995 at.% Si, and Al–0.96 at.% Sc, Al–3 at.% Zr and Al–78 at.% Er master alloys. The two alloys, referred to in this paper as Er-free and Er-containing alloys, were cast into a cast-iron mold preheated to 200 °C. Their compositions in the as-cast state are given in Table 1, as measured by direct current plasma emission spectroscopy (DCPMS) (ATI Wah Chang, Albany, OR). The impurity Fe concentration was 0.006 at.% for both alloys.

The cast alloys were homogenized in air at 640 °C for 72 h and then water quenched to ambient temperature. A two-stage aging treatment of 4 h at 300 °C followed by 8 h at 425 °C, denoted in the following as peak-aging, was employed to achieve peak strength and coarsening resistance, as explained above. The second-stage temperature of 425 °C was selected so that the final aging temperature was higher than the creep testing temperature of 400 °C.

2.2. Microstructure observations

The microstructures of samples polished to a 1 μm surface finish were imaged by SEM using a Hitachi S3400N-II microscope equipped with an Oxford Instruments INCAx-act detector for energy-dispersive X-ray spectroscopy (EDS). Polished specimens were then etched for 30 s, using Keller's reagent to reveal their grain boundaries. Vickers microhardness measurements were performed on a Duramin-5 microhardness tester (Struers), using a 200 g load applied for 5 s on samples polished to a 1 μm surface finish. Fifteen indentations were made per specimen across several grains.

Specimens for three-dimensional local-electrode atom-probe (LEAP) tomography were prepared by cutting blanks with a diamond saw to dimensions of $0.35 \times 0.35 \times 10\ mm^3$. These were electropolished at 8–20 V DC using a solution of 10% perchloric acid in acetic acid, followed by a solution of 2% perchloric acid in butoxyethanol at room temperature. Pulsed-voltage APT was performed with a LEAP 4000X Si X tomograph (Cameca, Madison, WI) [24–29] at a specimen temperature of 35 K, employing a pulse repetition rate of 250 kHz, a pulse fraction of 20% and an evaporation rate of 0.04 ions per pulse. LEAP tomographic data were analyzed with the IVAS 3.4.1 software program (Cameca). The matrix/precipitate heterophase interfaces were delineated with Al isoconcentration surfaces, and compositional profiles were obtained by the proximity histogram (proxigram) methodology [30,31]. The measurement errors for all quantities were calculated based on counting statistics and standard error propagation techniques [32].

Previous attempts to measure Si concentrations in Al by LEAP tomography resulted in measured values that are smaller than both the expected nominal value and the value

Table 1
Compositions (at.%) of the alloys investigated, as measured by DCPMS and LEAP tomography of peak-aged alloys; measurement uncertainty is given in parenthesis after the significant digit to which it applies.

Nominal	Measured alloy composition (DCPMS)				Measured alloy composition (LEAP)			
	Si	Zr	Sc	Er	Si^{2+}	Zr	Sc	Er
Al–0.06Zr–0.06Sc–0.04Si	0.036(1)	0.062(1)	0.059(1)	–	0.0211 (3)	0.0441 (5)	0.0583 (5)	–
Al–0.06Zr–(0.05Sc–0.01Er)–0.04Si	0.033(1)	0.056(1)	0.046(1)	0.011(1)	0.0347 (3)	0.0412 (5)	0.0434 (5)	0.0044 (5)

measured by DCPMS [33,34]. LEAP tomography measured Si concentrations in a similar study of Al–Sc–Li–Yb–Si alloys [34] were shown to be incorrect because of an artifact in the spatial detection of Si, which segregates at low-index crystallographic poles, owing to surface migration of the Si atoms during pulsed evaporation. The Si atoms are then preferentially retained with respect to Al until the atomic terraces evaporate completely. For the LEAP tomographic operating conditions employed, which were the same as those used in Ref. [34], Si evaporates exclusively as $^{28}Si^{2+}$, whose peak in the mass spectrum lies in the decay tail of the $^{27}Al^{2+}$ peak, further reducing the accuracy of the concentration measurement. As in previous research [34], the Si^{2+} concentration is reported, and is measured to be less than both the nominal and DCPMS measured values (Table 1).

2.3. Creep experiments

Constant load compressive creep experiments were performed at 400 ± 1 °C on cylindrical samples with diameter 10 mm and height 20 mm. The samples were heated in a three-zone furnace, and the temperature was verified by a thermocouple placed within 1 cm of the specimen. The samples were placed between boron nitride-lubricated alumina platens and subjected to uniaxial compression by Ni superalloy rams in a compression creep frame using dead loads. Sample displacement was monitored with a linear variable displacement transducer with a resolution of 6 μm, resulting in a minimum measurable strain increment of 3×10^{-4}. When a measurable steady-state displacement rate was achieved for a suitable duration, the applied load was increased. Thus, a single specimen yielded minimum creep rates for a series of increasing stress levels, at the end of which the strain did not exceed 11%. Strain rates at a given load were obtained by measuring the slope of the strain vs time plot in the secondary or steady-state creep regime.

3. Results

3.1. Microstructure

The microstructures of the peak-aged Er-free and Er-containing alloys are displayed in Fig. 1a and b, respectively. The grains in both alloys are elongated radially along the cooling direction, with smaller grains at the center of the billet, as expected for cast alloys. The Er-containing alloy has smaller grains than the Er-free alloy, with a larger grain density of 2.1 ± 0.2 compared with 0.5 ± 0.1 grains mm^{-2}, as determined by counting grains in the billet cross sections. The finer grain structure in the Er-containing alloy is due to intergranular Al_3Er precipitates with trace amounts of Sc and Zr, with diameters of ~2 μm, visible in Fig. 1c, and with compositions verified by semi-quantitative EDS. These particles inhibit grain growth after solidification and/or during homogenization. Such primary precipitates were not observed in the Er-free alloy, indicating that the solubility limit of the Er-containing alloy was exceeded during solidification and heat-treatment, as observed previously in Al–0.06Zr–0.04Sc–0.02Er (at.%) [1]. The addition of Sc and Zr has thus significantly decreased the 0.046 at.% solubility of Er in a binary Al–Er alloy [35]. The Er concentration, as measured by LEAP tomography of the peak-aged Er-containing alloy, is 0.0044 ± 0.0005 at.%. Thus, less than half the nominal value of 0.01 at.% Er is available for nanoscale precipitates formed on aging, while the remainder is present in the coarser primary Al_3Er precipitates. The Er-containing alloy also contains submicron intragranular Al_3Er precipitates, Fig. 1c, which is probably a result of microsegregation during solidification. The first solid to form in dilute Al–Zr–Sc–Er alloys is enriched in Zr, resulting in a microstructure consisting of Zr-enriched dendrites surrounded by Sc and Er-enriched interdendritic regions. Previous research on as-cast arc-melted Al–0.06Zr–0.06Sc and Al–0.1Zr–0.1Sc (at.%) alloys revealed microsegregation of both Sc and Zr using linear composition profiles obtained with quantitative electron-probe microanalysis [36,37]. In summary, the presence of Al_3Er primary precipitates refines the grain size and reduces the effective Er concentration available for strengthening nanoscale precipitation. In the following, the nominal compositions are used to label the alloys.

3.2. Nanostructure of peak-aged alloys

The nanostructures of the Er-free and Er-containing alloys, after aging isothermally for 4 h at 300 °C and 8 h at 425 °C, are compared employing LEAP tomography in Fig. 2. The spheroidal precipitates in the Er-free alloy consist of a Sc-enriched core surrounded by a Zr-enriched shell (Fig. 3). The precipitates have an average radius of 2.4 ± 0.5 nm, a number density of $2.5 \pm 0.5 \times 10^{22}$ m^{-3} and a volume fraction of 0.259 ± 0.007% (Table 2). The spheroidal precipitates in the Er-containing alloy consist of a core enriched in both Er and Sc, surrounded by a Zr-enriched shell with an average radius $\langle R \rangle$ of 2.3 ± 0.5 nm, a number density N_v of $2.0 \pm 0.3 \times 10^{22}$ m^{-3} and a volume fraction ϕ of 0.280 ± 0.006%. Silicon partitions to the precipitate phase and shows no preference for the precipitate core or shell in either alloy.

The precipitate and matrix compositions of the two alloys (Table 3) demonstrate that all alloying additions (Si, Zr, Sc and Er) partition to the precipitate phase. The matrix of the Er-containing alloy is more depleted of solute, with a composition of 107 ± 12 at.ppm Zr, 32 ± 4 at.ppm Sc and -7 ± 4 at.ppm Er, than that of the Er-free alloy, with a composition of 153 ± 28 at.ppm Zr, 89 ± 14 at.ppm Sc; the negative Er concentration is a result of a background correction and should be interpreted as 0, within measurement accuracy. Given the difficulties in measuring accurately the concentration of Si with LEAP tomography, and given that Si does not affect the precipitated volume

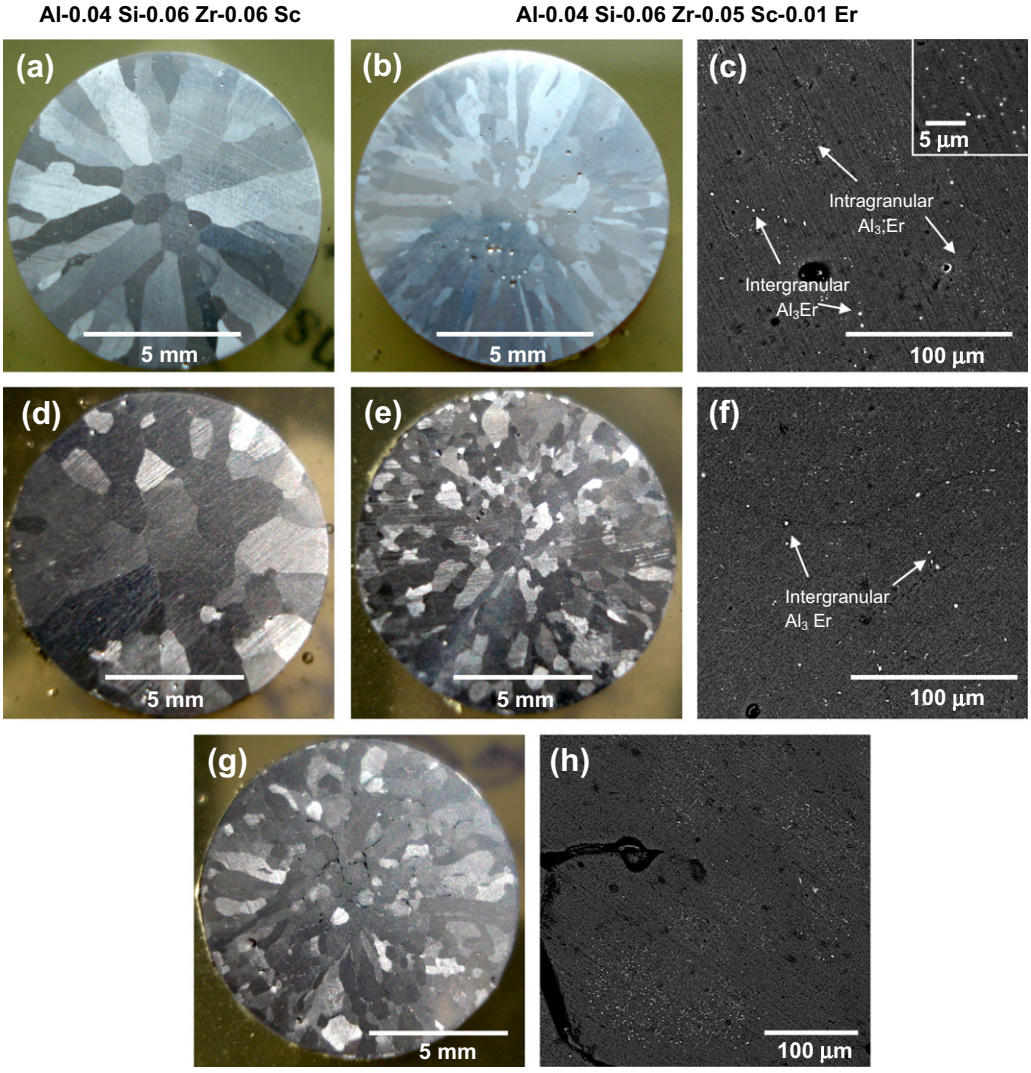

Fig. 1. Optical and SEM micrographs of cross sections for (a) Al–0.06Zr–0.06Sc–0.04Si and (b) Al–0.06Zr–(0.05Sc–0.01Er)–0.04Si, following a two-stage peak-aging treatment (4 h/300 °C and 8 h/425 °C). The Er-containing alloy has smaller grains, with a grain density of 2.1 ± 0.2 grains mm^{-2}, owing to the presence of (c) intergranular Al_3Er precipitates with trace amounts of Sc and Zr, as verified by semi-quantitative EDS. The Er-free alloy has 0.5 ± 0.1 grains mm^{-2} and no intergranular precipitates. After creep at 400 °C, the grain size of Al–0.06Zr–0.06Sc–0.04Si is (d) 0.6 ± 0.1 grains mm^{-2}. The grains in the Er-containing alloy after creep (e) have recrystallized, resulting in an increase in the grain density to 3.6 ± 0.2 grains mm^{-2}, and the intergranular and intragranular Al_3Er precipitates remain (f). Grain boundary void formation and coarsening of the intragranular Al_3Er precipitates are evident after creep at 400 °C for 1045 h, (g) and (h). The grains are larger compared with the Er-containing sample crept for 123 h, with a smaller grain density of 3.1 ± 0.2 compared with 3.6 ± 0.2 grains mm^{-2}.

fraction because it substitutes on the Al sublattice site of the ordered trialuminides [23,38], the analysis focuses on the precipitate-forming elements (Zr, Sc and Er), which provide ambient and elevated temperature precipitation strengthening.

3.3. Room and elevated temperature mechanical properties

3.3.1. Peak-aged condition

The as-cast microhardness values of the Er-free and Er-containing alloys are 256 ± 4 and 270 ± 8 MPa, respectively. These microhardness values are larger than those of previous as-cast dilute Al–Sc–X alloys, with comparable solute contents, of 210–240 MPa. The larger microhardness values may be evidence of early-stage clustering or precipitation, possibly as a result of the addition of Si, which has been shown to accelerate precipitate nucleation in an Al–0.06Zr–0.06Sc (at.%) alloy aged at 300 °C [23]. After homogenization and peak aging, the microhardness values of the present alloys increase to 627 ± 10 and 606 ± 20 MPa, respectively. To determine the operating coherent precipitate strengthening mechanism in the alloys, the strength increments for order strengthening ($\Delta\sigma_{ord}$), coherency and modulus strengthening ($\Delta\sigma_{coh} + \Delta\sigma_{mod}$) or strengthening by the Orowan bypass mechanism ($\Delta\sigma_{Or}$) are calculated using the equations given in the Appendix, and are listed in Table 4. The predicted strengthening increments are compared with the measured strength increment,

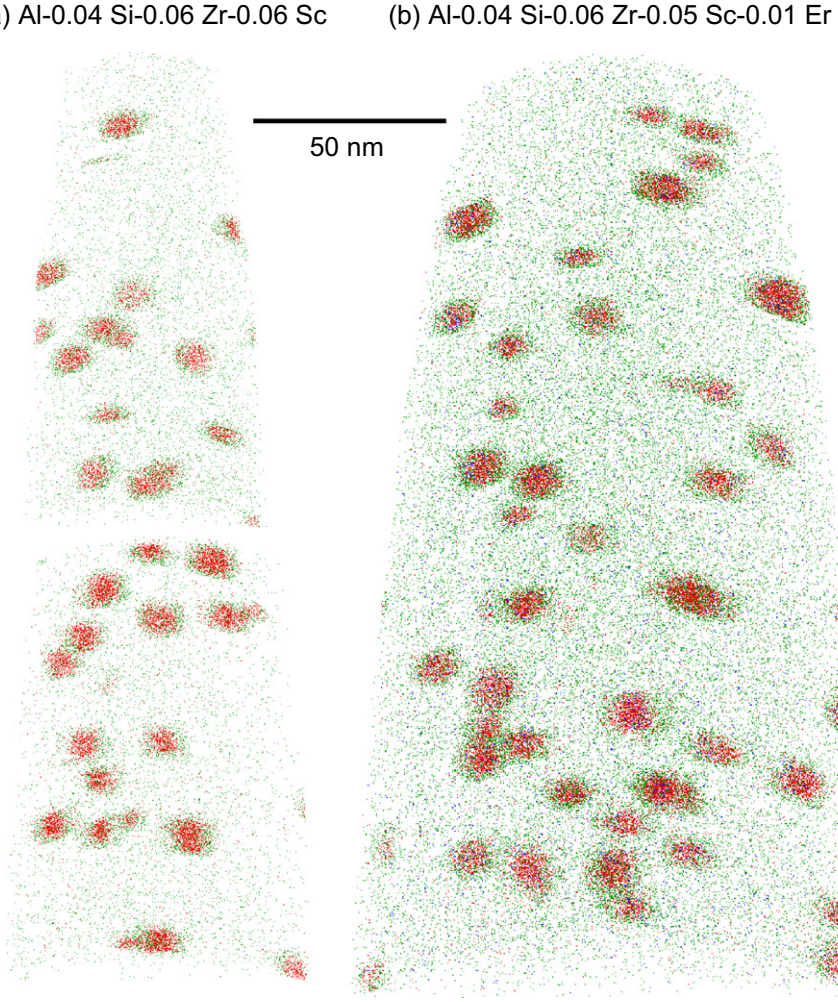

Fig. 2. APT reconstructions of alloys after a two-stage peak-aging treatment (4 h/300 °C and 8 h/425 °C): (a) Al–0.06Zr–0.06Sc–0.04Si (with two different specimens to improve precipitate counting statistics); (b) Al–0.06Zr–(0.05Sc–0.01Er)–0.04Si. Scandium atoms are displayed in red, Zr atoms in green, Er atoms in blue, illustrating the core–shell structure. Aluminum and Si atoms are omitted for clarity. (For interpretation of the references to color in this figure legend, the reader is referred to the web version of this article.)

estimated as $\Delta HV/3$ [39], where ΔHV is the increase in microhardness from the as-quenched state to the peak-aged state. The strengthening increment from precipitate shearing is taken as the larger of (a) the sum of modulus strengthening and coherency strengthening or (b) the order strengthening. This is because the mechanisms in (a) and (b) occur sequentially as dislocations move towards the matrix/precipitate interface and shear the precipitates. Shearing and Orowan bypass occur in parallel (i.e., dislocations either shear or bypass the precipitates), so strengthening is dictated by the mechanism that requires the smallest stress. The critical radius at which the deformation mechanism changes from precipitate shearing to an Orowan bypass mechanism in the Al–Sc system is 1.5–2.0 nm in an Al–0.18 at.% Sc alloy [40,41]. Accordingly, for the two peak-aged alloys studied here, with average precipitate radii of 2.3 ± 0.5 and 2.4 ± 0.5 nm, the Orowan bypass mechanism is predicted to be operative, as indicated by numerical results (Table 4). Note that good agreement between the measured and predicted Orowan strength increments was previously reported for Al–0.06 at.% Sc alloys with and without additions of Zr, Ti, Gd, Tb, Dy, Ho, Er, Tm, Yb, Lu and Li [18,34,40,42–46].

Fig. 4 displays the minimum compressive strain rate vs uniaxial compressive stress at 400 °C for the two alloys tested in the peak-aged condition. The apparent stress exponent for dislocation climb-controlled creep for the Er-free alloy (measured over the range 7–13 MPa) is 16 ± 1, which is significantly greater than that of 4.4 expected for Al [47]. Larger than expected stress exponents were previously measured in other Al–Sc-based alloys [17,40,41,45,48–51] and are indicative of a threshold stress for creep, below which dislocation creep is not measureable in laboratory time-frames. To determine the threshold stress for dislocation creep σ_{th}^{disloc}, the dislocation creep data are analyzed with a modified version of the Mukherjee–Bird–Dorn creep equation:

$$\dot{\varepsilon} = A(\sigma - \sigma_{th}^{disloc})^n \exp\left(\frac{-Q}{k_B T}\right) \quad (1)$$

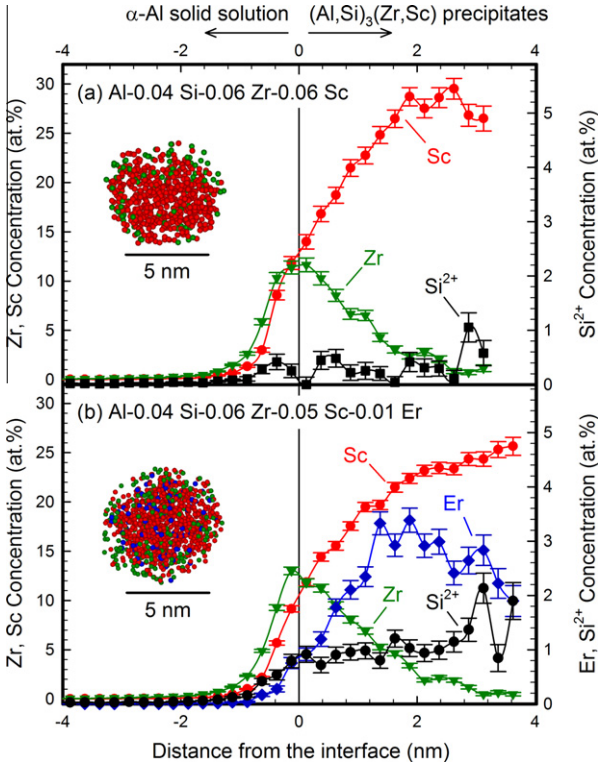

Fig. 3. Average concentration profiles (proximity histograms) across the matrix/precipitate interface for alloys after a two-stage peak-aging treatment (4 h/300 °C and 8 h/425 °C): (a) Al–0.06Zr–0.06Sc–0.04Si; (b) Al–0.06Zr–(0.05Sc–0.01Er)–0.04Si. Precipitates exhibit a Zr-rich shell and a core enriched in Sc (and Er), and Si partitions to the precipitates without preference for the core or the shell. The inset images in (a) and (b) are APT reconstructions of a representative precipitate from each alloy with same color scheme as in Fig. 2. (For interpretation of the references to color in this figure legend, the reader is referred to the web version of this article.)

Table 2
Precipitate number density N_v, mean radius $\langle R \rangle$, volume fraction ϕ and Vickers microhardness HV of the alloys studied.

Alloy	N_v ($\times 10^{22}$ m^{-3})	$\langle R \rangle$ (nm)	ϕ (%)	HV (MPa)
Al–0.06Zr–0.06Sc–0.04Si	2.5 ± 0.5	2.4 ± 0.5	0.259 ± 0.007	627 ± 10
Al–0.06Zr–(0.05Sc–0.01Er)–0.04Si (peak-aged[a])	2.0 ± 0.3	2.3 ± 0.5	0.280 ± 0.006	606 ± 20
Al–0.06Zr–(0.05Sc–0.01Er)–0.04Si (over-aged[b])	0.2 ± 0.1	5–10	–	436 ± 10

[a] 4 h/300 °C and 8 h/425 °C.
[b] Peak-aged and 1045 h/400 °C.

where A is a constant, σ is the applied stress, and n and Q are the stress exponent and activation energy for diffusion in pure aluminum. The threshold stress is obtained from a linear least-squares regression of $\sqrt[n]{\dot{\varepsilon}}$ vs. σ, with a weight of $1/\sigma^2 \sqrt[n]{\dot{\varepsilon}}$, where $\sigma \sqrt[n]{\dot{\varepsilon}}$ is the uncertainty in the nth root of the strain rate. The value of σ_{th}^{disloc} is calculated by dividing the value of the y-axis intercept of the linear regression analysis by its slope. Applying Eq. (1) to the data for the Er-free alloy and using $n = 4.4$ yields a threshold stress of 6.5 ± 0.5 MPa for the Er-free alloy (Table 5).

The Er-containing alloy exhibits two creep regimes (Fig. 4), which are identified as diffusional creep at lower stresses and dislocation climb controlled creep at higher stresses. The grain size in the Er-containing alloy is sufficiently small for diffusional creep to occur at 400 °C, which is a homologous temperature of 0.72 T_m (where T_m is the absolute melting point of Al, 934 K). The apparent stress exponent for diffusional creep, as measured between 8 and 9 MPa, is 6 ± 1, indicative of a threshold stress for diffusional creep σ_{th}^{diff}. This is calculated from a modified version of the Mukherjee–Bird–Dorn creep equation identical to Eq. (1), though the values of A and Q are specific to diffusional creep, and $n = 1$. The resulting value of σ_{th}^{diff} of 6.9 ± 0.8 MPa has a significant uncertainty, beyond the error bar of 0.8 MPa, given that only three data points were available for the best-fit procedure. At higher stresses, dislocation creep becomes the dominant deformation mechanism in the Er-containing alloy, with an apparent stress exponent of 20 ± 2 (11–15 MPa), indicating a threshold stress for dislocation creep. Fitting the dislocation creep data to Eq. (1) yields a threshold stress of 9.3 ± 0.7 MPa.

The microstructures of the two alloys following creep testing at 400 °C are displayed in Fig. 1d and e, respectively. After creep at 400 °C, the grains in the Er-free alloy (Fig. 1d) appear unchanged with 0.6 ± 0.1 grains mm^{-2}, compared with the 0.5 ± 0.1 grains mm^{-2} before creep (Fig. 1a). The grains in the Er-containing alloy following creep (Fig. 1e) have undergone recrystallization, resulting in an increase in the grain density to 3.6 ± 0.2 grains mm^{-2} from the pre-creep value of 2.1 ± 0.2 (Fig. 1b). The intergranular Al_3Er precipitates remain following creep (Fig. 1f).

3.3.2. Over-aged condition

To collect more data in the diffusional creep regime of the Er-containing alloy, a second series of creep experiments was performed at 400 °C on another peak-aged sample, beginning at a lower applied stress of 6 MPa. Compressive creep data were collected over 325 h for four stresses ranging from 6 to 8.5 MPa, which yielded a nearly constant strain rate of $1.2 \pm 0.2 \times 10^{-8}$ s^{-1}, where the error is the standard deviation of the four resulting strain rates. A constant strain rate for increasing applied stress is indicative of an evolving microstructure, that is, grain growth during the creep test. Since the rate of diffusional creep at a given stress decreases with increasing grain size, grain growth can account for the nearly constant strain rate measured between 6 and 8.5 MPa.

The applied stress was then removed, and the sample was held in the creep frame for 48 h at 400 °C to allow for a full recovery of the dislocation microstructure. Creep testing of the sample, by then at 400 °C for 373 h (15.5 days), and labeled in the following as 'over-aged', was then resumed, beginning at a stress of ~6 MPa and lasting 672 h (28 days), most of it spent below 13 MPa.

Table 3
Compositions of the precipitates and matrix in peak-aged alloys (4 h/300 °C and 8 h/425 °C).

Alloy	Precipitate composition (at.%)				Matrix composition (at.ppm)			
	Zr	Si^{2+a}	Sc	Er	Si^{2+a}	Zr	Sc	Er
Al–0.06Zr–0.06Sc–0.04Si	4.23 ± 0.15	0.35 ± 0.04	25.29 ± 0.31	–	163 ± 24	153 ± 28	89 ± 14	–
Al–0.06Zr–(0.05Sc–0.01Er)–0.04Si	3.31 ± 0.08	1.75 ± 0.06	21.28 ± 0.17	2.43 ± 0.07	294 ± 12	107 ± 12	32 ± 4	−7 ± 4

[a] The reported Si concentrations are inaccurate, owing to difficulties in quantifying Si in Al with the LEAP tomographic technique (Section 2.2).

Table 4
Experimental ($\Delta HV/3$) and calculated strength increments (Eqs. (A1)–(A4)) for peak-aged alloys.

Alloy	$\Delta HV/3$ (MPa)	$\Delta\sigma_{ord}$ (MPa) (Eq. (A1))	$\Delta\sigma_{coh} + \Delta\sigma_{mod}$ (MPa) (Eqs. A2, A3)	$\Delta\sigma_{Or}$ (MPa) (Eq. (A4))
Al–0.06Zr–0.06Sc–0.04Si	124 ± 4	120 ± 1	151 ± 8	134 ± 39
Al–0.06Zr–(0.05Sc–0.01Er)–0.04Si (peak-aged[a])	112 ± 7	124 ± 1	166 ± 9	143 ± 44
Al–0.06Zr–(0.05Sc–0.01Er)–0.04Si (over-aged[b])	55 ± 10	124 ± 1	215–273	52–86

[a] 4 h/300 °C and 8 h/425 °C.
[b] Peak-aged and 1045 h/400 °C.

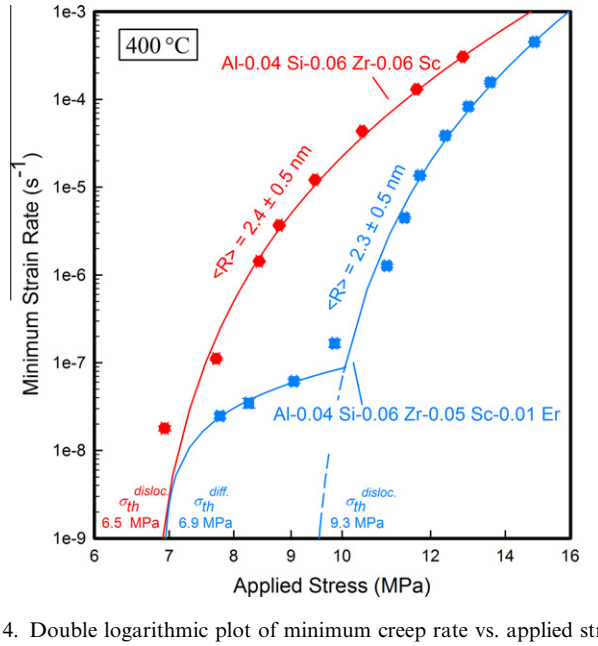

Fig. 4. Double logarithmic plot of minimum creep rate vs. applied stress for compressive creep experiments at 400 °C for: (a) Al–0.06Zr–0.06Sc–0.04Si; (b) Al–0.06Zr–(0.05Sc–0.01Er)–0.04Si after a two-stage peak-aging treatment (4 h/300 °C and 8 h/425 °C). Best fit lines to Eq. (1) are plotted, and resulting threshold stresses for diffusional σ_{th}^{diff} and dislocation σ_{th}^{disloc} creep are shown, where applicable.

The results of this series of tests on the over-aged sample are shown in Fig. 5, and compared with those obtained for the peak-aged alloy. For all measured stresses, the creep rates of the over-aged Er-containing alloy are lower than in the peak-aged condition, in some cases by about three orders of magnitude. In the dislocation creep regime at high stresses (14–18 MPa), an apparent stress exponent of 29 ± 2 is again indicative of a threshold stress, which is determined as 13.9 ± 1.6 MPa. In the diffusional creep regime at low stresses (6–11 MPa), the apparent stress exponent is 2.5 ± 0.2, and the threshold stress is 4.5 ± 0.8 MPa. A transition region between diffusional and dislocation creep between 11 and 13 MPa is observed, which was not present in the peak-aged sample.

The microstructure of the over-aged alloy after a total of 1045 h (43.5 days) in the creep frame at 400 °C is displayed in Fig. 1g. There is evidence of void formation at the grain boundaries, and of significant coarsening of the intragranular Al_3Er precipitates compared with the peak-aged state (Fig. 1b). The formation of voids may be due to tensile stresses developing perpendicular to the applied compressive load, resulting from slight barreling of the sample during compressive creep testing. It is likely that these voids formed after considerable strain had accumulated in the sample, and they may thus affect the last few creep data points measured at the highest stresses, resulting in higher

Table 5
Comparison of the experimental normalized threshold stresses for dislocation creep $\sigma_{th}^{disloc}/\Delta\sigma_{Or}$ measured on peak-aged alloys with those predicted by a threshold stress model for Al–Sc-based alloys [22], which accounts for average precipitate radius $\langle R\rangle$ and unconstrained lattice parameter misfit δ; all values are given for a temperature of 400 °C.

Alloy	Creep time at 400 °C (h)	$\langle R\rangle$ (nm)	δ (%)	σ_{th}^{disloc} Experimental (MPa)	$\Delta\sigma_{Or}$ Eq. (A1) (MPa)	$\sigma_{th}^{disloc}/\Delta\sigma_{Or}$ Experimental (%)	$\sigma_{th}^{disloc}/\Delta\sigma_{Or}$ Modeled [22] (%)
Al–0.06Zr–0.06Sc–0.04Si	130	2.4 ± 0.5	0.55	6.5 ± 0.5	111 ± 34	5.9 ± 1.8	17
Al–0.06Zr–(0.05Sc–0.01Er)–0.04Si	123	2.3 ± 0.5	0.82	9.3 ± 0.7	119 ± 35	7.8 ± 2.4	29

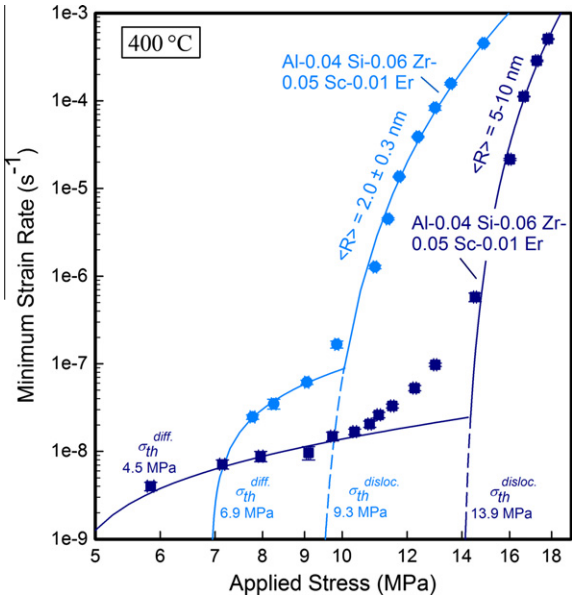

Fig. 5. Double logarithmic plot of minimum creep rate vs. applied stress for compressive creep experiments at 400 °C for Al–0.06Zr–(0.05Sc–0.01Er)–0.04Si (a) after a two-stage peak-aging treatment (4 h/300 °C and 8 h/425 °C) and (b) after subsequent exposure at 400 °C for 325 h at applied stresses ranging from 6 to 8.5 MPa. Best fit lines to Eq. (1) are plotted, and resulting threshold stresses for diffusional σ_{th}^{diff} and dislocation, σ_{th}^{disloc} creep are shown, where applicable.

than expected strain rates. The over-aged sample exhibits a microhardness of 436 ± 10 MPa, following 1075 h of creep at 400 °C, which is, as anticipated, below the peak-aged value of 606 ± 20 MPa.

The grains are slightly larger in the Er-containing alloy that was exposed for 1045 h at 400 °C, with a larger grain density of 3.1 ± 0.2 grains mm^{-2}, compared with the 3.6 ± 0.2 grains mm^{-2} from the Er-containing sample exposed for 123 h. LEAP tomographic analysis of the crept material (reconstructions not shown) revealed a number density of precipitates of $2 \pm 1 \times 10^{21}$ m^{-3}, where the high degree of error is because only five precipitates were detected in a 50 million atom data set, all of which were only partially bound by the tip volume. Given the poor precipitate statistics, detailed compositional and structural analyses are not possible, though the precipitate radius was estimated from the LEAP tomographic reconstruction to be 5–10 nm. Assuming that the volume fraction of precipitates is constant for the peak-aged and over-aged sample, and using the measured number density of $2 \pm 1 \times 10^{21}$ m^{-3}, a radius of 6–9 nm is calculated for the spheroidal precipitates, in good agreement with the above estimate.

4. Discussion

4.1. Precipitate structure

Precipitates with a structure consisting of an Er- and Sc-enriched core surrounded by a Zr-enriched shell (core/shell structure) are formed in the peak-aged Er-containing alloy (Fig. 3). A previous study on an Al–0.06Zr–0.04Sc–0.02Er (at.%) alloy yielded precipitates with a structure consisting of an Er-enriched core surrounded by a Sc-enriched inner shell and a Zr-enriched outer shell (core/double-shell structure) after either isothermal aging at 400 °C or isochronal aging to 450 °C in stages of 25 °C h^{-1} [1]. The core/double-shell structure was shown by first-principles calculations to be the most energetically favorable precipitate structure for dilute Al–Zr–Sc–Er alloys [52], and to form by sequential precipitation of solute elements according to their intrinsic diffusivities D, where $D_{Er} > D_{Sc} > D_{Zr}$ at 400 °C [1]. No diffusion data are available for Er in Al at 400 °C, although the evidence of accelerated precipitation kinetics in the Al–Zr–Sc system due to addition of Er suggests that the diffusivity of Er in Al is larger than that of Sc at 400 °C [1]. The lack of a core/double-shell structure in the present Er-containing alloy must therefore be a result of either the different aging treatment used or the addition of Si. The first-stage aging treatment of 4 h at 300 °C is designed to precipitate Er and Sc out of solution as rapidly as possible to minimize both processing time and precipitate coarsening. The diffusivity of Er at 300 °C, $D_{Er} = 4 \pm 2 \times 10^{-19}$ m^2 s^{-1}, as determined from Al_3Er ($L1_2$) coarsening experiments in a binary Al–0.045 at.% Er alloy [35], is ~4 ± 2 times greater than that of Sc in binary Al–Sc, $D_{Sc} = 9.1 \times 10^{-20}$ m^2 s^{-1} at 300 °C [53]. The addition of Si to the base alloy studied here may have accelerated the precipitation kinetics of Sc, as it has been shown to do in an Al–0.06Si–0.06Zr–0.06Sc alloy at 300 °C [23], thereby decreasing the difference between D_{Er} and D_{Sc}, and resulting in co-precipitation of Er and Sc into Al_3(Sc,Er) precipitates of uniform composition. The subsequent aging at 425 °C then creates a Zr-rich Al_3(Sc,Zr) shell. A precipitate structure consisting of a co-precipitated Yb- and Sc-enriched core, with evidence at the matrix/precipitate interface of Zr-enrichment (which was deemed to not constitute a shell), was previously found for an Al–0.02Zr–0.06Sc–0.02Yb (at.%) alloy aged for 1536 h at 300 °C [54]. This is in contrast to the Yb-enriched core/Sc-enriched shell structure observed in an Al–0.06Sc–0.005 Yb (at.%) alloy aged at 300 °C [35,44]. The precipitate structure observed in Al–Zr–Sc–RE alloys, be it core/shell or core/double-shell, is clearly sensitive to the aging treatments and alloying additions employed, a subject that warrants serious future investigations.

After aging, the volume fraction of precipitates is larger and the total matrix solute concentration smaller in the Er-containing alloy compared with the Er-free alloy (Tables 2 and 3). This is evidence for increased precipitation kinetics due to the addition of Er and was observed previously in dilute Al–Zr–Sc alloys and attributed to differences in the intrinsic diffusion coefficients ($D_{Er} > D_{Sc} > D_{Zr}$) [1]. Similar effects have been observed in previous studies of Al–0.06Sc at.% alloys with 0–0.02 at.% RE element additions of Er, Yb, Gd, Ho, Lu, Tm or Tb [18,35,42,44,46].

Finally, it is emphasized that the degree of coarsening observed in the crept Er-containing alloy after 44 days at

400 °C was not observed in a previous alloy with a similar composition (Al–0.06Zr–0.04Sc–0.02Er (at.%)) aged isothermally for a longer time, 64 days, at 400 °C. In the previous study, the precipitate radius of 3.7 ± 0.3 nm after 0.5 h at 400 °C remained unchanged within uncertainly after 64 days, with a value of 3.8 ± 0.4 nm. The increased coarsening behavior observed here is probably the result of either the applied stress during creep, as observed previously in Al alloys [55–57], and/or the addition of Si, which has been demonstrated to accelerate precipitation kinetics [23,33,38].

4.2. Creep behavior

4.2.1. Diffusional creep

Diffusional creep is observed in the peak-aged Er-containing alloy, where primary Al_3Er precipitates result in a fine-grained microstructure after casting and aging (Fig. 1b and c). Diffusional creep was not reported in previous creep studies of cast dilute Al–Sc-based alloys, where the grain sizes were on the order of 1–2 mm [17,40,41,45,48–51], such as those in the Er-free alloy studied here. A threshold stress for diffusional creep of 6.9 ± 0.8 MPa is measured in the peak-aged Er-containing alloy, and is most likely due to the intergranular primary Al_3Er precipitates (Fig. 1c). Threshold stresses for diffusional creep in alloys have been attributed to limitations in the ability of grain boundaries to act as perfect sources and sinks for vacancies, owing to the presence of intergranular second-phase particles [58–60]. These particles were modeled to impede the movement of grain boundary dislocations, limiting vacancy condensation on the boundary and controlling the rate of diffusional creep. It is emphasized that diffusional creep can be eliminated in the Er-containing alloy by reducing the Er concentration to 0.005 at.%, the effective alloy composition measured by LEAP tomography (Fig. 1), eliminating intergranular Al_3Er precipitates and increasing the alloy grain size. Recrystallization occurs only in the crept Er-containing alloy, which has significantly finer grains than those of the Er-free alloy, and thus more energy stored in the metal, and a larger driving force for recrystallization [61].

The decrease in the rates of diffusional creep in the over-aged sample (Fig. 5) is expected due to grain growth that occurred during over-aging, which lasted 325 h under applied stresses ranging from 6 to 8.5 MPa. The decrease in the threshold stress for diffusional creep from 6.9 ± 0.8 to 4.5 ± 0.8 after over-aging is anticipated from the coarsening of the intergranular Al_3Er precipitates, decreasing the number of obstacles to grain boundary sliding.

4.2.2. Dislocation creep

Fig. 4 shows that the resistance to dislocation creep of the alloy containing 0.01 at.% Er is significantly greater than that of the Er-free alloy, with the same average precipitate radius, within experimental error (Table 2). The experimentally measured threshold stress for dislocation creep in dilute Al–Sc-based alloys increases with increasing lattice parameter mismatch between the matrix and precipitates [51]. These findings agree with the predictions of models that attribute the threshold stress to elastic interactions between dislocations and the coherent precipitates with lattice parameter- and shear modulus-mismatches with the matrix that they bypass by dislocation climb [21,22]. The constrained lattice parameter mismatches at 400 °C are calculated to be 0.55% and 0.82% for the Er-free and Er-containing alloys, respectively, by linear interpolation of lattice parameter data for $L1_2$-ordered $Al_3(Sc, Er)$ and $Al_3(Sc, Zr)$, [62,63], using the experimentally measured precipitate compositions, and adjusted for thermal expansion of $Al_3(Sc, Er)$ and $Al_3(Sc, Zr)$ [64] and Al [65]. The impact of Si on the lattice parameter is neglected, owing to the difficulties in measuring accurately the Si concentration from LEAP tomography (Section 2.2), and the lack of experimental data on the lattice parameter of $(Al,Si)_3Sc$.

The threshold stresses expected for the alloys studied here are calculated employing a recent model by Krug and Dunand [22], which attributes the existence of a threshold stress to an attractive interaction force between precipitates and the dislocations that climb over them. This model builds on the general climb model developed by Rösler and Arzt [66] for creep in alloys strengthened by coherent, unshearable precipitates, and its extension by Marquis and Dunand [21] to include elastic interactions between dislocations and precipitates due to lattice parameter and shear modulus mismatches between the matrix and precipitates. In the model developed by Krug and Dunand [22], as dislocations climb over a precipitate by vacancy-mediated diffusion, they become trapped close to the apex of a precipitate by elastic stresses induced in the matrix due to a lattice parameter mismatch with it. The application of an externally applied stress, the threshold stress, produces a shear force that allows the dislocation to escape and dislocation creep to continue. This model predicts that the threshold stress, when normalized to the Orowan stress (the stress at which dislocations bypass the precipitates by looping), increases with increasing precipitate radius and/or increasing lattice parameter misfit. These predictions are validated qualitatively by experimental creep results in dilute Al–Sc-based alloys at 300 °C [17,40,41,45,48–51], as summarized in Ref. [51]. Using the above model [22], normalized threshold stresses of 0.17 and 0.29 (that is, threshold stresses of 17% and 29% of the Orowan stress) are predicted for the peak-aged Er-free and Er-containing alloys. The calculated values are larger than those measured experimentally of 0.059 ± 0.018 and 0.078 ± 0.024, respectively (Table 5). An overestimate of the threshold stresses by a similar factor of 2–3 was also observed earlier [22] for threshold stresses in Al–Sc, Al–Sc–Li and Al–Sc–Yb alloys at 300 °C, and was argued to be because of the geometry of individual precipitates, the overall precipitate arrangement, and the fact that the shapes of the climbing dislocation are more complex than accounted for by the simple analytical model. Note that

the predicted Orowan stress at 400 °C (Table 5) is smaller than the value at room temperature (Table 4), owing to the temperature dependence of the shear modulus of Al.

The increase in the threshold stress for dislocation creep in the Er-containing alloy from the peak- to over-aged state can be explained by the observed increase in the precipitate radius from 2.3 ± 0.5 nm for the peak-aged state to 5–10 nm for the over-aged alloy. The normalized threshold stress for the Er-containing alloy increases by a factor of 2–3 from 0.08 ± 0.02 to 0.16–0.27, and the radius increases by a factor of 2–4 from 2.3 ± 0.5 to 5–10 nm (Fig. 6). The same nearly linear increase in the measured threshold stress for dislocation creep with increasing radius was found in many other dilute Al–Sc-based alloys at 300 °C [17,40,41,45,48–51], as summarized in Ref. [51], in qualitative agreement with the predictions of the model by Krug and Dunand [22].

4.2.3. Comparison with other castable, creep-resistant Al alloys

Dilute Al–Sc, Al–Sc–RE and Al–Sc–Li alloys are not sufficiently coarsening resistant to be considered for creep applications at 400 °C, but they have excellent creep resistance between 300 and 350 °C [17,34,40,41,45,48–51]. Comparisons of the creep behavior at 400 °C between the present alloys and several highly coarsening-resistant Al–Sc–Zr, Al–Sc–Ti, Al–Zr and Al–Zr–Ti alloys, however, can be made. A 7 MPa threshold stress for dislocation creep was determined at 400 °C for an Al–0.06Zr–0.06Sc (at.%) alloy aged isochronally to 400 °C, for which neither precipitate radius nor lattice parameter data are available. This threshold stress is in excellent agreement with the value of 6.5 ± 0.5 MPa measured here for the peak-aged Er-free alloy with a similar composition (Al–0.06Zr–0.06Sc–0.04Si (at.%)), indicating that the precipitate radius and composition in the previous study were comparable with those measured here. A threshold stress of 10 ± 3 MPa was measured at 400 °C for an Al–0.06Sc–0.06 Ti (at.%) alloy with an average precipitate radius of 8.3 ± 2.9 nm and a lattice parameter mismatch of 0.72%. The threshold stress in this Al–Sc–Ti alloy is larger than that measured here for the Er-containing alloy (Fig. 6), probably because of the larger precipitates, and is also larger than that of the Er-free alloy, because both the precipitate radius and lattice parameter misfit are larger (Table 5). Finally, threshold stresses of 6–7 MPa were measured at 400 °C for Al–0.1 Zr and Al–0.1 Zr–0.1 Ti (at.%) alloys isothermally aged for 100 h at 400 °C. The precipitate volume fraction and average radius in these alloys are not well defined, owing to solute segregation to the dendrites, and significant intergranular precipitation [50], preventing further comparison.

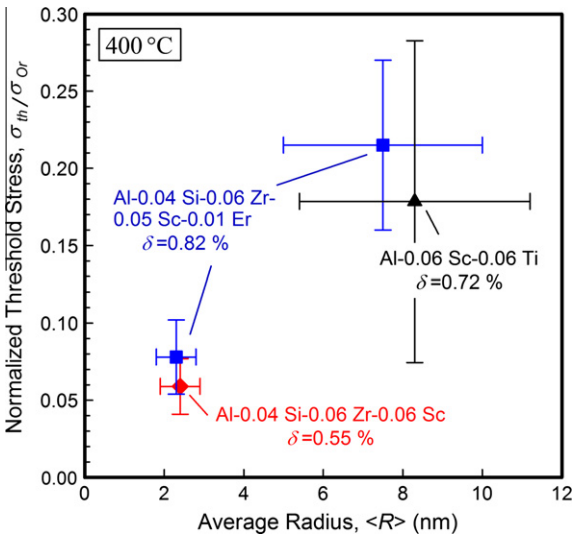

Fig. 6. Plot of threshold stresses for dislocation creep at 400 °C normalized to the Orowan stress vs average precipitate radius $\langle R \rangle$ for the alloys studied here. The result for an Al–0.06Sc–0.06Ti (at.%) alloy is also shown [45].

5. Conclusions

The effect of substituting 0.01 at.% Er for Sc in an Al–0.06Zr–0.06Sc–0.04Si (at.%) alloy subjected to a two-stage peak-aging treatment of 4 h at 300 °C and 8 h at 425 °C was assessed to determine the viability of dilute Al–Zr(–Sc/Er)–Si alloys for high-temperature, low-stress, applications. The following conclusions are reached.

1. The effective Er concentration of the Al–0.06Zr–(0.05Sc–0.01Er)–0.04Si (at.%) alloys was diminished by a factor of ~2, owing to the formation of inter- and intragranular primary Al_3Er ($L1_2$) precipitates. The Er-containing alloy has finer grains, with a larger grain density of 2.1 ± 0.2 grains mm^{-2} compared with 0.5 ± 0.1 grains mm^{-2} for the Er-free alloy, owing to the intergranular Al_3Er precipitates that inhibit grain growth.
2. Coherent, spheroidal, $L1_2$-ordered, nanometric, trialuminide precipitates consisting of an Er- and Sc-enriched core and a Zr-enriched outer shell were formed in the Er-containing alloy, providing excellent creep and coarsening resistance.
3. At ambient temperature, the Orowan bypass mechanism is predicted to be operative for both Er-free and Er-containing alloys, which have average precipitate radii of 2.4 ± 0.5 and 2.3 ± 0.5 nm, respectively, after peak aging.
4. The addition of 0.01 at.% Er significantly improves the resistance of the alloys to dislocation creep at 400 °C, increasing the threshold stress σ_{th}^{disloc} from 7 to 9 MPa. Increasing the precipitate radius from 2 to 5–10 nm further increases the threshold stress of the Er-containing alloy to 14 MPa. Both results agree with experimental observations of increasing values of σ_{th}^{disloc} with increasing lattice parameter misfit and increasing precipitate radius in dilute Al–Sc–RE-based alloys. These findings also agree with the qualitative predictions of a model that attributes the existence of a threshold stress in

Al–Sc-based alloys to an attractive interaction force between precipitates and the dislocations that climb over them [22].

5. Diffusional creep is observed in the Er-containing alloy at 400 °C due to the finer-grained microstructure that results from intergranular Al_3Er ($L1_2$) precipitates. Decreasing the alloy concentration of Er to ~0.005 at.% will eliminate these intergranular precipitates, resulting in grain sizes on the order of 1–2 mm and disappearance of diffusional creep at laboratory time scales, while maintaining the improved resistance to dislocation creep imparted by the nanoscale, coherent, spheroidal, $L1_2$-ordered precipitates.

Acknowledgements

This research was sponsored by the Ford–Boeing–Northwestern University Alliance (81132882). APT was performed at the Northwestern University Center for Atom-probe Tomography (NUCAPT). The LEAP tomography system was purchased and upgraded with funding from NSF-MRI (DMR-0420532) and ONR-DURIP (N00014-0400798, N00014-0610539 and N00014-0910781) grants. The authors also gratefully acknowledge the Initiative for Sustainability and Energy at Northwestern (ISEN) for grants to upgrade the capabilities of NUCAPT. They thank Prof. P. Sanders, Mr N. Johnson and Mr P. Quimby (Michigan Technological University) for casting the alloys, Dr M. Krug (NU) for many useful discussions and for modeling the normalized threshold stress, Mr M. Diaz (NU) for his help with SEM and Dr D. Isheim for his assistance with LEAP tomography. Dr J. Boileau (Ford), Dr B. Ghaffari (Ford), Mr C. Huskamp (Boeing) and Dr K.K. Sankaran (Boeing) are thanked for many useful discussions.

Appendix A

The strength increments for order strengthening ($\Delta\sigma_{ord}$), coherency and modulus strengthening ($\Delta\sigma_{coh} + \Delta\sigma_{mod}$), and strengthening by the Orowan bypass mechanism ($\Delta\sigma_{Or}$), are calculated employing the methodology described [67,68], as performed previously [37,40,42,43]. First, the contribution to the yield strength from order strengthening is given by

$$\Delta\sigma_{ord} = 0.81M\frac{\gamma_{APB}}{2b}\left(\frac{3\pi\phi}{8}\right)^{1/2} \tag{A1}$$

where $M = 3.06$ is the mean matrix orientation factor for aluminum [69], $b = 0.286$ nm is the magnitude of the matrix's Burgers vector [47], ϕ is the volume fraction of precipitates, and $\gamma_{ABP} = 0.5\ J\ m^{-2}$ is an average value of the Al_3Sc anti-phase boundary (APB) energy for the (1 1 1) plane [70–72].

The increase is yield strength due to coherency strengthening is given by

$$\Delta\sigma_{coh} = M\alpha_\varepsilon(G\varepsilon)^{3/2}\left(\frac{\langle R\rangle\phi}{0.5Gb}\right)^{1/2} \tag{A2}$$

where $\alpha_\varepsilon = 2.6$ is a constant [67], $\langle R\rangle$ is the mean precipitate radius, $G = 25.4$ GPa [47] is the shear modulus of Al, and ε is the constrained lattice parameter mismatch obtained using Vegard's law and the precipitate compositions measured here.

Strengthening by modulus mismatch is given by

$$\Delta\sigma_{mod} = 0.0055M(\Delta G)^{3/2}\left(\frac{2\phi}{Gb^2}\right)^{1/2} b\left(\frac{\langle R\rangle}{b}\right)^{\left(\frac{3m}{2}-1\right)} \tag{A3}$$

where $\Delta G = 42.5$ GPa is the shear modulus mismatch between the matrix and the precipitates [73], and m is a constant, taken to be 0.85 [67].

Finally, the increase in yield strength for the Orowan bypass mechanism is given by

$$\Delta\sigma_{Or} = M\frac{0.4}{\pi}\frac{Gb}{\sqrt{1-v}}\frac{\ln\left(\frac{2r}{b}\right)}{\lambda} \tag{A4}$$

where $v = 0.34$ is the Poisson's ratio of the matrix [69], and λ is the edge-to-edge inter-precipitate distance, which is taken to be the square lattice spacing in parallel planes [74]:

$$\lambda = \left[\left(\frac{3\pi}{4\phi}\right)^{1/2} - 1.64\right]\langle R\rangle \tag{A5}$$

References

[1] Booth-Morrison C, Dunand DC, Seidman DN. Acta Mater 2011;59:7029.
[2] Elagin VI, Zakharov VV, Pavlenko SG, Rostova TD. Phys Met Phys Metall 1985;60:97.
[3] Tolley A, Radmilovic V, Dahmen U. Scr Mater 2005;52:621.
[4] Forbord B, Lefebvre W, Danoix F, Hallem H, Marthinsen K. Scr Mater 2004;51:333.
[5] Clouet E, Lae L, Epicier T, Lefebvre W, Nastar M, Deschamps A. Nat Mater 2006;5:482.
[6] Clouet E, Nastar M, Sigli C. Phys Rev B 2004;69:064109.
[7] Fuller CB, Murray JL, Seidman DN. Acta Mater 2005;53:5401.
[8] Fuller CB, Seidman DN. Acta Mater 2005;53:5415.
[9] Toropova LS, Eskin D, Kharakterova M, Dobatkina T. Advanced aluminum alloys containing scandium: structure and properties. Amsterdam: Gordon & Breach Science; 1998.
[10] Clouet E, Nastar M, Barbu A, Sigli C, Martin G. Adv Eng Mater 2006;8:1228.
[11] Clouet E, Nastar M, Barbu A, Sigli C, Martin G. In: Howe JM, Laughlin DE, Lee JK, Dahmen U, Soffa WA, editors. Solid-solid phase transformations in inorganic materials. Warrendale, PA: TMS; 2005. p. 1.
[12] Lefebvre W, Danoix F, Hallem H, Forbord B, Bostel A, Marthinsen K. J Alloys Compd 2009;470:107.
[13] Clouet E, Barbu A, Lae L, Martin G. Acta Mater 2005;53:2313.
[14] Hallem H, Lefebvre W, Forbord B, Danoix F, Marthinsen K. Mater Sci Eng A 2006;A421:154.
[15] Royset J, Ryum N. Int Mater Rev 2005;50:19.
[16] Karnesky RA, Dunand DC, Seidman DN. Acta Mater 2009;57:4022.
[17] Karnesky RA, Seidman DN, Dunand DC. Mater Sci Forum 2006;519–521:1035.
[18] Karnesky RA, van Dalen ME, Dunand DC, Seidman DN. Scr Mater 2006;55:437.
[19] Hedrick JB. US Geological Survey 2007 minerals yearbook: rare earths. Reston, VA: USGS; 2007.

[20] Zalutskaya OI, Ryabov VR, Zalutskii II. Dopov Akad Nauk Ukr RSR, Ser A 1969;31:255.
[21] Marquis EA, Dunand DC. Scr Mater 2002;47:503.
[22] Krug ME, Dunand DC. Acta Mater 2011;59:5125.
[23] Booth-Morrison C, Mao Z, Wolverton C, Dunand DC, Seidman DN. Acta Mater, in preparation.
[24] Bajikar SS, Larson DJ, Kelly TF, Camus PP. Ultramicroscopy 1996;65:119.
[25] Kelly TF, Camus PP, Larson DJ, Holzman LM, Bajikar SS. Ultramicroscopy 1996;62:29.
[26] Kelly TF, Larson DJ. Mater Charact 2000;44:59.
[27] Seidman DN. Rev Sci Instrum 2007;78:030901/1.
[28] Seidman DN. Annu Rev Mater Res 2007;37:127.
[29] Kelly TF, Miller MK. Rev Sci Instrum 2007;78:031101/1.
[30] Hellman OC, Vandenbroucke JA, Rusing J, Isheim D, Seidman DN. Microsc Microanal 2000;6:437.
[31] Hellman OC, Blatz du Rivage J, Seidman DN. Ultramicroscopy 2003;95:199.
[32] Parratt LG. Probability and experimental errors in science. New York: John Wiley; 1966.
[33] Beeri O, Dunand DC, Seidman DN. Mater Sci Eng A 2010;A527:3501.
[34] Krug ME, Dunand DC, Seidman DN. Acta Mater 2011;59:1700.
[35] van Dalen ME, Karnesky RA, Cabotaje JR, Dunand DC, Seidman DN. Acta Mater 2009;57:4081.
[36] Knipling KE, Dunand DC, Seidman DN. Acta Mater 2011;59:943.
[37] Knipling KE, Karnesky RA, Lee CP, Dunand DC, Seidman DN. Acta Mater 2010;58:5184.
[38] Du G, Deng J, Wang Y, Yan D, Rong L. Scr Mater 2009;61:532.
[39] Tabor D. Brit J Appl Phys 1956;7:159.
[40] Seidman DN, Marquis EA, Dunand DC. Acta Mater 2002;50:4021.
[41] Marquis EA, Seidman DN, Dunand DC. Acta Mater 2003;51:285.
[42] Krug ME, Werber A, Dunand DC, Seidman DN. Acta Mater 2009;58:134.
[43] Fuller CB, Seidman DN, Dunand DC. Acta Mater 2003;51:4803.
[44] van Dalen ME, Dunand David C, Seidman David N. J Mater Sci 2006;41:78814.
[45] van Dalen ME, Seidman DN, Dunand DC. Acta Mater 2008;56:4369.
[46] Karnesky RA. Ph.D. thesis, Northwestern University, Evanston, IL; 2007.
[47] Frost H, Ashby M. Deformation mechanism maps. Oxford: Pergamon Press; 1982.
[48] Fuller CB, Seidman DN, Dunand DC. Scr Mater 1999;40:691.
[49] Marquis EA, Seidman DN, Dunand DC. Acta Mater 2003;51:4751.
[50] Knipling KE, Dunand DC. Scr Mater 2008;59:387.
[51] Krug ME, Seidman D. N., Dunand DC. Acta Mater, submitted for publication.
[52] Mao Z, Booth-Morrison C, Seidman DN, Wolverton C. Acta Mater, in preparation.
[53] Fujikawa S. Diffus Defect Data, Pt A 1997;143–147:115.
[54] van Dalen ME, Gyger T, Dunand DC, Seidman DN. Acta Mater 2011;59:7615.
[55] Murken J, Girard O, Hohner R, Skrotzki B, Eggeler G. Mater Sci Forum 2000;331–337:1507.
[56] Nakajima T, Takeda M, Endo T. Mater Sci Eng A 2004;A387–A389:670.
[57] Skrotzki B, Murken J. Lightweight alloys for aerospace application, proceedings of [a] symposium held at the TMS annual meeting, New Orleans, LA, United States; February 12–14, 2001, 2001:52.
[58] Harris JE. Metal Sci J 1973;7:1.
[59] Ashby MF. Scr. Met. 1969;3:837.
[60] Burton B. Mater Sci Eng 1972;10:9.
[61] Shewmon PG. Transformation in metals. New York: McGraw-Hill; 1969.
[62] Harada Y, Dunand DC. Intermetallics 2008;17:17.
[63] Harada Y, Dunand DC. Mater Sci Eng A 2002;A329–A331:686.
[64] Harada Y, Dunand DC. Scr Mater 2003;48:219.
[65] Royset J, Ryum N. Scr Mater 2005;52:1275.
[66] Rösler J, Arzt E. Acta Metall 1988;36:1043.
[67] Ardell AJ. Metall Trans A 1985;16A:2131.
[68] Argon A. Strengthening mechanisms in crystal plasticity. Oxford: Oxford University Press; 2007.
[69] Meyers M, Chawla K. Mechanical metallurgy: principles and applications. Paramus, NJ: Prentice-Hall; 1984.
[70] Fu CJ. Mater Res 1990;5:971.
[71] George E, Pope D, Fu C, Schneibel J. ISIJ Int 1991;31:1063.
[72] Fukunaga K, Shouji T, Miura Y. Mat Sci Eng 1997;A239:202.
[73] Hyland R, Stiffler R. Scr Metall Mater 1991;25:473.
[74] Nembach E. Particle strengthening of metals and alloys. New York, NY: John Wiley; 1997.